Geothermal Energy

RESEARCH

Open Access

Thermal modeling and simulation of a single-flash geothermal power plant involving non-condensable gas: a case study of Kamojang geothermal field in Garut, West Java, Indonesia

Candra Mecca Sufyana, Fiki Taufik Akbar and Wahyu Srigutomo*

*Correspondence:
srigutomo@itb.ac.id

Physics of Earth and Complex System, Physics Department, Faculty of Mathematics and Natural Sciences, Institut Teknologi Bandung, Jl. Ganesha 10, Bandung 40132, Indonesia

Abstract

The presence of non-condensable gases (NCGs) in a geothermal fluid disrupts the vacuum process in the condenser, reducing turbine efficiency and decreasing the total power output of the geothermal power plant (GPP). Therefore, to optimize the thermodynamic efficiency of a GPP, NCGs should be removed using a gas removal system. Since there is a substantial lack of design and simulation software for a GPP including NCG removal alternatives, in this study, we aimed to model and develop a software-based interface to simulate mass and energy balance involving an NCG fraction in a single-flash GPP as well as examine the thermodynamic performance of the gas removal system, which is the most important step in the planning and designing phase of a GPP. This software was validated using outputs of Kamojang GPP Units 2, 3, and 4 located at Kamojang geothermal field, Garut, West Java, Indonesia. Units 2 and 3 use two ejectors which are installed in series, and Unit 4 utilizes a hybrid system (HS) that is mostly a combination of vacuum pumps and a steam jet ejector (SJE). Our results showed that Kamojang GPP Units 2 and 3 generate 55.295 MW of power with an absolute error of 0.53%, whereas Unit 4 generates 60.218 MW of power with a 0.36% absolute error concerning the field data. These results correspond with the expected minimum error; therefore, our model's parameters are considered valid and can be used for simulation. We found that using the simulation, the total steam saved by the HS at Kamojang GPP Units 2 and 3 was 534 kW. Furthermore, the net power production was reduced by 1.6% for the HS and 2.03% for the SJE with every 1% increase in the NCG fraction. The power requirement of the vacuum pumps remained less than the power generated by the motive steam which the ejector requires to dispose of the same amount of NCG, indicating that Kamojang GPP Units 2 and 3 will be more efficient if an HS is used.

Keywords: Single-flash geothermal power plant, Thermodynamic efficiency, Non-condensable gases, Gas removal system, Software-based interface

Introduction

The Kamojang geothermal field, located in Garut, West Java, Indonesia (Fig. 1), was developed by Pertamina and is estimated to have a potential capacity of 300 MW. The Kamojang geothermal power plant (GPP) has adopted a single-flash system whose current installed capacity is 235 MW and which consists of five generating units. Unit 1 has a capacity of 30 MW; Units 2 and 3 have a capacity of 55 MW and are operated by PT. Indonesia Power and Unit 4 and 5 have a capacity of 60 MW and 35 MW, respectively, and are operated by PT. Pertamina Geothermal Energy. One of them in the Kamojang area is a small-scale GPP of 3 MW owned by the Agency for the Assessment and Application of Technology Indonesia (BPPT). In a single-flash GPP, the fluid at the wellhead is a saturated liquid (Ameri et al. 2006) which is passed into a flasher (separator) to separate the liquid and vapor phases. During the flashing process, the fluid pressure decreases, causing a decrease in temperature and vapor fraction. At this condition, enthalpy remains constant, while entropy increases. The steam generated from the flasher is directed into a turbine to generate electricity, while the remaining liquid is reinjected into the reinjection well.

Figure 2 shows the list diagram of the research steps. First, the initial data and research hypotheses were defined. Second, the governing equations for each segment were separately derived. Third, the proposed model was developed using the Visual Basic programming language in accordance with the first two steps, and finally, according to the modeling, the output results were shown and the selection of a gas removal system at the Kamojang GPP was discussed.

Geothermal fluids have a relatively high content of non-condensable gases (NCGs). The NCG is typically composed of CO_2, H_2S, NH_3, CH_4, N_2, and C_2H_6, with CO_2

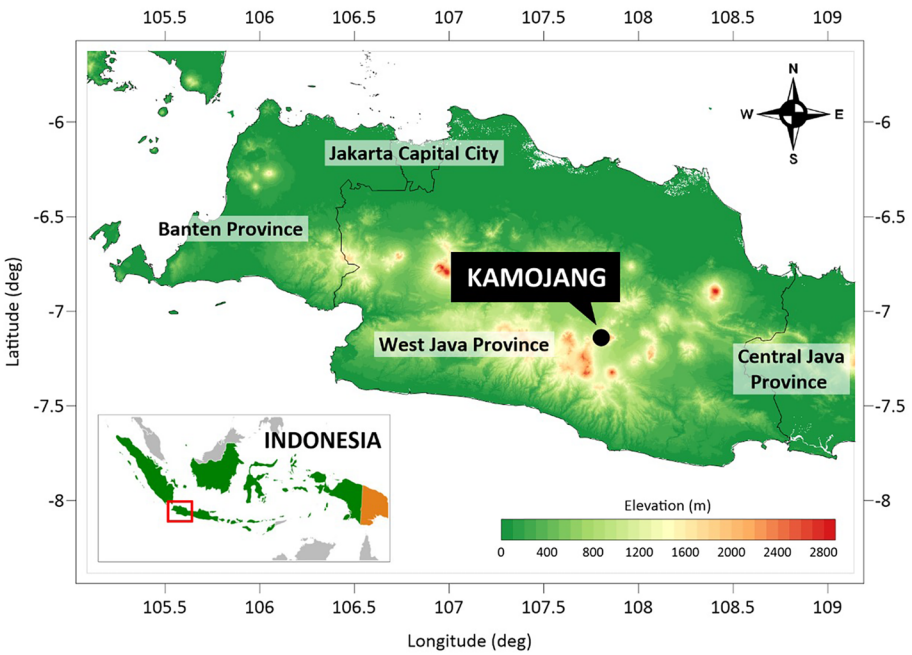

Fig. 1 Location map of Kamojang geothermal power plant in Garut, West Java, 40 km southeast of Bandung, Indonesia; it is located in a high-altitude area of 1500 masl and on the geographical coordinates 07°11′02″–07°06′08″ S and 107°44′36″–107°49′30″ E

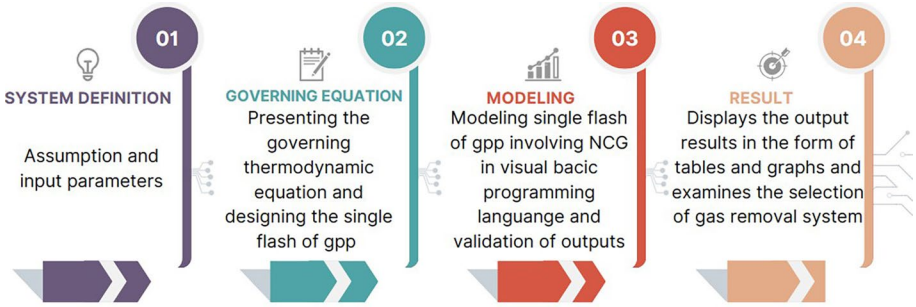

Fig. 2 List diagram of the steps taken in this study

making up more than 85% of the content (Michaelides 1982). Numerous studies have examined the energy analysis of GPPs, but they only took NCG into account in the gas extraction system and not in the full cycle (DiPippo and Marcille 1984; DiPippo 1992, 1994, 2004; Cadenas 1999; Cerci 2003; Siregar 2004; Kwambai 2005; Aqui et al. 2005; Dagdas et al. 2005; Ozturk et al. 2006; Kanoglu et al. 2007). Khalifa and Michaelides (1978) conducted the initial research on the impact of NCGs on the effectiveness of GPPs. According to their study, the network output dropped by up to 20–25% when geothermal steam containing 10% by weight of CO_2 was used compared to when clean steam was used. The number of NCGs present in geothermal steam has a substantial impact on a GPP's ability to generate electricity (DiPippo 2015; Sulistyardi 2010; Zarrouk and Moon 2014). The fraction of NCG varies worldwide depending on the resource, from near nil to as high as 25% by weight of steam (Hall 1996; Coury et al. 1996). Currently, the NCG content in the Kamojang geothermal field is approximately 0.5% to 1.7% (Wahyuningsih et al. 2005). Michaelides (1980) constructed a flash system at a wellhead and selected the flash temperature based on the NCG content to separate the NCGs before they enter the turbine. If the NCG content is high, it is advised that while designing plants, NCG separation should be considered both thermodynamically and economically (Tajima and Nomura 1982; Montero 1990; Yildirim and Gokcen 2004).

The amount of NCG in the condenser could be reduced using a gas removal system. The cost of the gas removal system in a geothermal system is high because of the elevated gas levels (Vorum and Fritzler 2000). The electricity produced is used to remove the NCG from the condensers and exhaust them into the atmosphere or into a system for abatement; this significantly reduces the efficiency of power generation (Duthie and Nawaz 1989). The conventional NCG removal systems are steam jet ejectors (SJE), liquid ring vacuum pumps (LRVP), centrifugal compressors, and hybrid systems (HS) (Millachine 2011). Michaelidas (1982) conducted a study to analyze the capabilities of various NCG removal systems and found that it is advisable to use an ejector when the NCG levels are relatively low and use an ejector compressor when they are high. Siregar (2004) examined LRVPs and SJE in one of his studies in order to improve the process by which power is generated in Indonesia's Sibayak geothermal field. He found that NCG was present in 3.07% by weight of steam, and the power consumed by the LRVP was estimated at 803 kW for a single-flash GPP

with a 20-MW capacity. Swandaru (2006) conducted similar research on Indonesia's Patuha geothermal field and found that NCG concentration was 1.77% in the field (by weight of steam). In a three-stage NCG removal system, the first two stages are SJE while the third is LRVP. Swandaru's study determined the steam consumption of SJEs and the power consumption of LRVP. Ozcan and Gokcen (2010) reported that thermodynamic simulation results for suitable usage of gas removal system (GRS) were recommended as the SJE used for NCG 0–2%, the HS used for NCG 2–10%, and the compressor for NCG > 10%. Marza (2011) stated that at a pressure of 0.08 bar in a steam condition of 0.5–1.5% NCG, the use of steam for the SJE and HS is almost the same. However, with a higher NCG content in the steam, almost three times as much motive steam is required for the steam jet than for the HS.

Various applications have been developed to simulate the mass and energy equilibrium of a GPP. The earliest was GEOCOST (Bloomster et al. 1975), which only includes the SJE and only applies to low NCG concentrations. Another is GETEM, which determines the performance of single-flash GPPs and only considers the SJE and LRVP as NCG removal systems (Chung et al. 2010). The most extensive and expensive software is ASPEN-HYSYS, a modeling tool for design, optimization, business planning, asset management, and monitoring of energy system performance. It is possible to create mass and energy balances with this software, but no information about the NCG removal system is obtained (Aspen-HYSYS 2010). Ozcan and Gokcen (2010) developed a code based on mass and energy balances using Engineering Equation Solver (EES). The absence of an NCG removal system in most GPP design and simulation software contributes substantially to less accurate results.

This research aimed to develop a software-based interface to determine a single-flash GPP (with particular emphasis on NCG) that maximizes power output, including mass and energy balances with steady-flow conditions and is quick and user-friendly. We created and developed a mass and energy balance modeling software involving NCG using Visual Basic programming language. This software was used to test the performance of GPP and conduct a study on GRS selection and was validated using the process flow diagram of Kamojang GPP Units 2, 3, and 4 located at Kamojang geothermal field, Garut, West Java, Indonesia. Units 2 and 3 use two ejectors installed in series. This type of gas removal requires a large amount of motive steam which can generate a lot of power when driving a turbine. The GPP requires motive steam of around 10500 kg/h or the equivalent of 1.5 MW, which is not a small amount. Unit 4 utilizes an HS which is mostly a combination of vacuum pumps and an SJE. Based on the results of thermodynamic and energy conversion models and simulations involving NCG at the GPP, we conducted a GRS selection study, including a study to replace the existing GRS with a hybrid-type GRS, with the hopes of improving the performance of the GPP. The scenarios were reviewed by the net Specific Steam Consumption (SSC), which is defined as the ratio between the amount of steam available and the power generated. An economic assessment is not within the scope of this study.

Thermodynamics model

Mass and energy balance

The initial design of a power plant begins with the selection of the corresponding thermodynamic cycle, construction of a power plant model, and determination of the

technical specifications for each component of the equipment through simulation. Every device is modeled using heat and mass balance (Siregar 2004; Moran et al. 2011; Pambudi et al. 2015). The first law of thermodynamics applies the principle of conservation of energy to systems in which heat transfer and work performance are methods of transferring energy. The main mass and energy balance equations used in the steady-state model are shown in Eq. 1 (Mohtaram et al. 2021, b; Omidi et al. 2019; Chen et al. 2021):

$$\dot{Q} - \dot{W} = \sum \dot{m}_e h_e - \sum \dot{m}_i h_i, \tag{1}$$

where $\dot{Q}$ is the sum of heat transferred into and out of the system, $\dot{W}$ is the net work done on the system, $\sum \dot{m}_e h_e$ is the output enthalpy rate to the control volume, and $\sum \dot{m}_i h_i$ is the input enthalpy rate to the control volume.

The flashing and separation processes

The temperature–entropy (T–S) diagram for a single-flash GPP is shown in Fig. 3. State 1 is a two-phase fluid with very high water content. State 2 is the flashing process in the separator. The flashing process is modeled under conditions of constant enthalpy, so it can be assumed that $h_1 = h_2$, where h_1 is the enthalpy at state 1 and h_2 is the enthalpy at state 2.

State 3 is the state of the water that has separated from the steam, and the separation process can be condensed at constant pressure as an isobaric process after the flash has occurred. State 4 is the entry point of the turbine in which the steam has

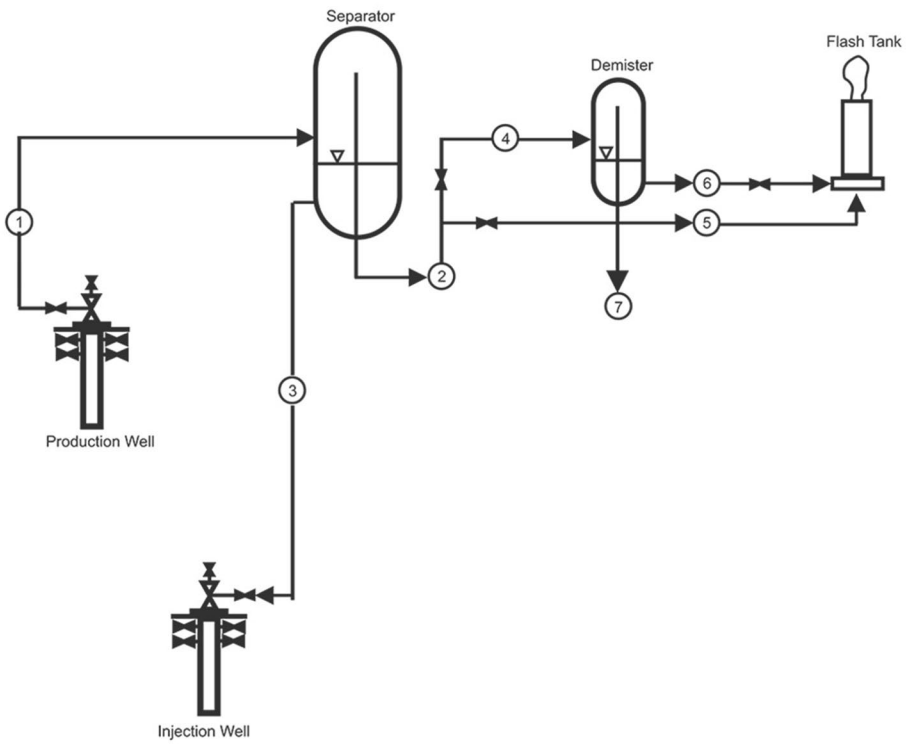

Fig. 3 Temperature–entropy (h–S) diagram for a single-flash power plant. Saturated water (h_3) and saturated steam (h_4) are created inside the separator. While brine, a liquid with a high enthalpy (h_3), is supplied to the reinjection wells, steam with a high enthalpy (h_4) is sent to the turbine (redrawn from DiPippo 2015)

separated from the water, while State 5 is the turbine's exit point; it is also the point of entry into the condenser. If this process is ideal, then the entropy of the steam when coming out of the turbine will be equal to that when it entered the turbine (isentropic) or the exit point of the turbine falls on state 5 s. The closer this process is to be isentropic, the higher the efficiency obtained will be. The condensation process occurs in the condenser, and the state of the fluid leaving the condenser is point 6; this is the state of saturated water. The temperature of the fluid at state 6 is further lowered in the cooling tower before finally being injected back into the earth through the condensate injection well.

Figure 4 shows the flow process of the separator, demister, and flash tank. The separation process is isobaric once the flash takes place. The pressures at states 1, 2, and 3 are equivalent and equal to the separator pressure ($P_1 = P_2 = P_3 = P_{separator}$), and the vapor quality at state 1 (x_1) can be expressed as:

$$x_1 = \frac{h_1 - h_3}{h_2 - h_3}. \tag{2}$$

Moreover, the mass flow rate of steam from the separator to the turbine ($\dot{m}_2$) is calculated as follows:

$$\dot{m}_2 = x_1 \dot{m}_1, \tag{3}$$

where $\dot{m}_1$ is the mass flow rate at state 2.

The mass flow rate of the fluid at state 4 ($\dot{m}_4$), which leaves the separator and leads to the demister, can be determined using Eq. 4:

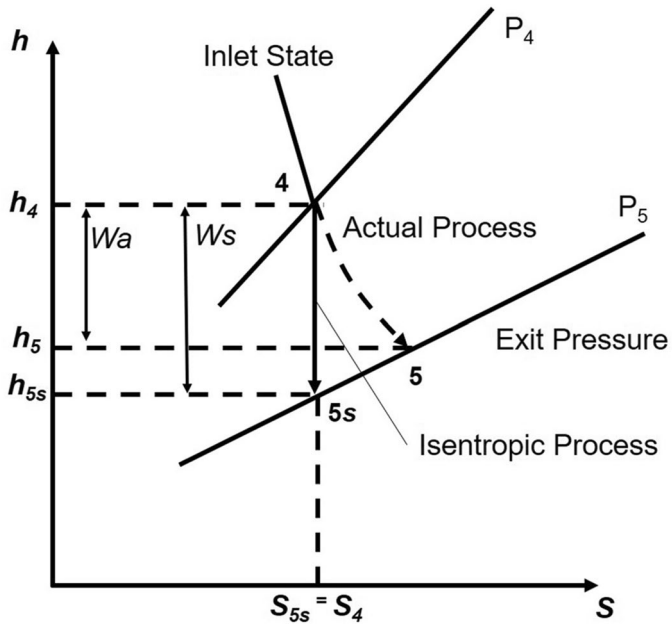

Fig. 4 Schematic diagram of a separator, demister, and flash tank. The separator ensures that only clean, dry steam enters the turbine; a demister is used to remove any leftover liquid droplets from steam, and a flash tank gathers a variety of condensate drain lines

$$\dot{m}_4 = \dot{m}_2 - \dot{m}_5, \tag{4}$$

where $\dot{m}_5$ is the mass flow rate at state 5.

The pressure loss occurring when the fluid passes through the demister is 10 kPa, and the flash mass flow rate is approximately 1% of the steam mass flow rate (Swandaru 2006). The mass flow of the fluid from state 7 ($\dot{m}_7$) to the turbine can then be determined using Eq. 5:

$$\dot{m}_7 = \dot{m}_2 - \dot{m}_6 = \dot{m}_2 - \left(0.01\dot{m}_4\right), \tag{5}$$

where $\dot{m}_6$ is the mass flow rate at state 6.

The turbine expansion process

The input condition of the working fluid and the exhaust pressure is set for a turbine in steady operation. The process is shown in Fig. 5 from state 4 to state 5 which is an ideal turbine process; this is the ratio of the actual work of the turbine to the work that occurs in the isentropic process. Isentropic efficiency of a turbine (η_t) is written as shown in Eq. 6:

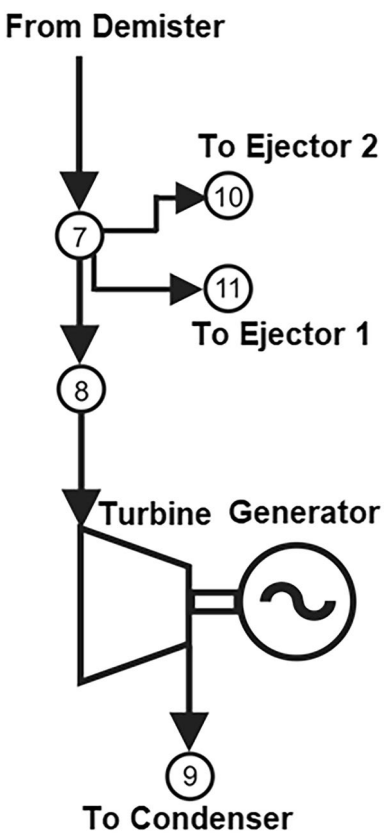

Fig. 5 h–S Diagram for the actual and isentropic processes of an adiabatic turbine. The isentropic process involves no irreversibility and serves as the ideal process for adiabatic devices (redrawn from Cengel and Boles 2018)

$$\eta_t = \frac{Actual\ turbine\ work}{Isentropik\ turbine\ work} = \frac{W_a}{W_s} = \frac{h_4 - h_{5a}}{h_4 - h_{5a,s}}, \tag{6}$$

where h_{5a} and $h_{5a,s}$ are the enthalpy values at the exit state for the actual and isentropic processes, respectively. According to Cengel and Boles (2018), the isentropic value of turbine condensation is determined by measuring the actual work output to measure the condition of the inlet and outlet pressures.

The turbine expansion flow process is shown in Fig. 6. An LRVP replaces the second-stage ejector in normal operation, allowing the second-stage ejector to be used as a redundancy. The work generated by the turbine per unit mass of steam results from the assumption that the processes taking place in the turbine are adiabatic and reversible (isentropic); the changes in the kinetic and potential energies when entering and exiting the turbine are neglected. The turbine generates energy in the form of Eq. 7, and the turbine's isentropic efficiency (w_t) is calculated as follows:

$$w_t = h_9 - h_8. \tag{7}$$

The turbine's isentropic efficiency (η_t) is calculated as follows:

$$\eta_t = \frac{h_8 - h_9}{h_8 - h_{9,s}}, \tag{8}$$

where $h_8, h_9, and h_{9,s}$ are enthalpy at states 8 and 9 and isentropic at state 9, respectively.

The mass flow of steam to the turbine ($\dot{m}_8$) is calculated using the following equation:

$$\dot{m}_8 = \dot{m}_7 - \dot{m}_{11}. \tag{9}$$

The steam quality at state 8 (X_8) is the same as that at state 7 (X_7), where the efficiency of the generator is η_g, the power of the turbine generator (W_g) is determined using Eq. 10 with W_t being turbine power:

$$W_g = \left(\frac{\eta_g}{\eta_t}\right) W_t = \left(\frac{\eta_g}{\eta_t}\right) X_8 \dot{m}_8 (h_8 - h_9). \tag{10}$$

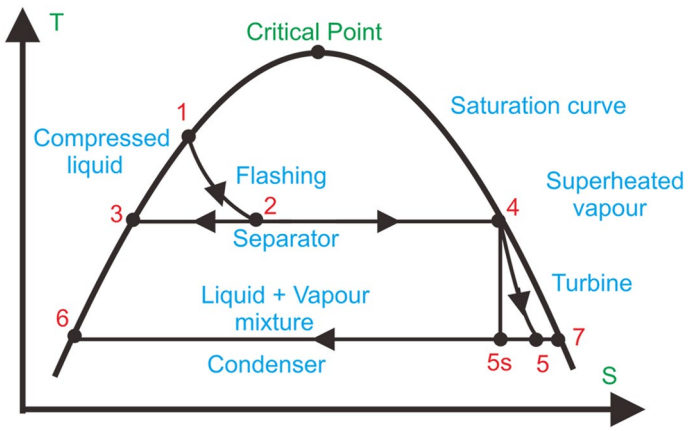

Fig. 6 The turbine expansion flow process. Steam from the demister (state 7) is used for the turbine and the steam ejectors of the first (state 11) second (state 10) stages

The condensing process

The function of a condenser is to condense incoming exhaust steam and provide a sub-atmospheric environment. The condenser pressure depends only on the amount of NCG present in the condenser and the maximum temperature reached by the cooling water. There are two types of condensers, namely the direct-contact and surface condensers; the most common type used in GPP is the direct-contact condenser (Siregar 2004). The flow diagram of a direct-contact condenser is shown in Fig. 7. The steam condenses on the water droplets, and the condensate flows through the barometric foot into a tank with a sealing hole to overcome atmospheric pressure. NCG and a small amount of steam is drawn from the condenser through the NCG exhaust system. Condenser pressure needs to be adjusted because of the gases that are dissolved in the cooling water. The extraction volume flow rate of condensable gas is higher than that of NCG. The new condenser pressure ($P_{con,x}$) is determined using Eq. 11:

$$P_{con,x} = P_{con}\left(1 + \frac{P_{NCG}}{P_{NCG} + P_{steam}}\right), \tag{11}$$

where P_{con} is the condenser pressure, P_{NCG} is the pressure of NCG, and P_{steam} is the pressure of steam.

Heat energy in the condenser (Q_{con}) can be calculated using Eq. 12:

$$Q_{con} = (h_{8'} - h_{9.1})\, \dot{m}_{8'}, \tag{12}$$

where $h_{8'}$ is enthalpy at state 8 after iterating using $P_{con,x}$, $m_{8'}$ is the mass flow rate at state 8 after deducting the mass flow rate used in the first-stage steam ejector, and $h_{9.1}$ is enthalpy to the hot well pump (HWP).

The condenser enthalpy (h_{con}) is calculated using Eq. 13:

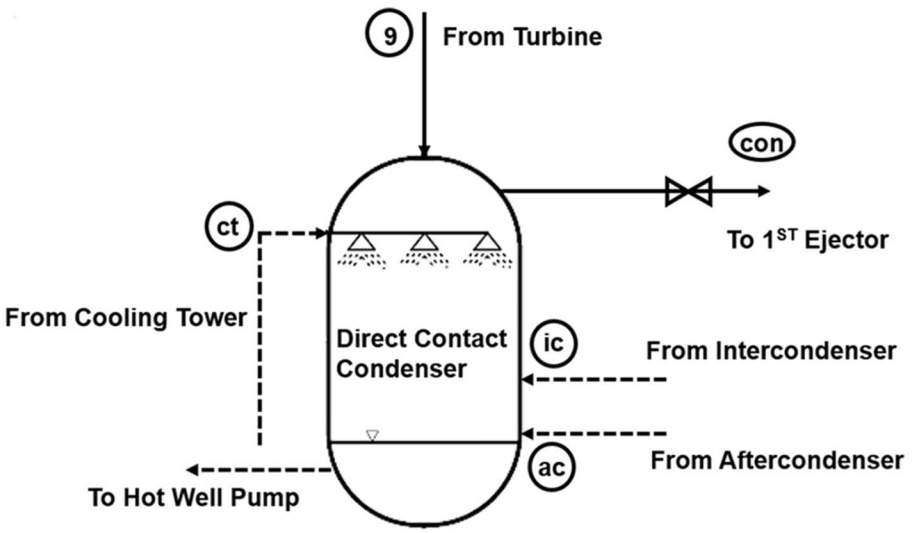

Fig. 7 Direct-contact condenser flow diagram. The steam leaving the turbine is directed into the condenser where it mixes with the cold-water spray from the cooling tower and the cooling gas from the NCG exhaust system

$$h_{con} = (h_{sep} - (\eta_t.(h_{sep} - h_{con,s})), \tag{13}$$

where $h_{con,s} = (h_{l,con} + (X_{con}(h_{v,con} - h_{l,con}))$ and $X_{con} = (s_{total} - s_{l,con})/(s_{v,con} - s_{l,con})$, h_{sep} is enthalpy at the separator, $h_{l,con}$ is liquid enthalpy at the condenser, $h_{v,con}$ is vapor enthalpy at the condenser, $s_{l,con}$ is liquid entropy at the condenser, $s_{v,con}$ is vapor–liquid at the condenser, and s_{total} is the entropy of the NCG (in this case, CO_2) obtained using an equation based on the function from temperatures 220–590 K. The equation of mass balance from the cooling tower ($\dot{m}_{ct}$) is as follows:

$$\dot{m}_{ct} = \frac{\dot{m}_{9v}(h_{9v} - h_{9.1}) + \dot{m}_{9CO_2}(h_9 - h_{con})_{CO_2} + \dot{m}_{ic}(h_{ic} - h_{9.1}) + \dot{m}_{ac}(h_{ac} - h_{9.1}) + \dot{m}_{con}(h_9 - h_{con})_v}{h_{9.1} - h_{ct}}, \tag{14}$$

where $\dot{m}_{con}$ is the mass flowrate at the condenser, $\dot{m}_{9CO_2}$ is the mass flow rate of carbon dioxide, $\dot{m}_{ic}$ the mass flowrate at the inter-condenser, and $\dot{m}_{ac}$ is the mass flow rate after the condenser.

The extraction gas system

To reduce the motive steam consumption of the ejector, the second-stage SJE can be replaced by a vacuum pump. The product of the integration of the SJE with the vacuum pump is usually called an HS. To calculate the power consumption required to clear a particular amount of saturated water vapor of an NCG from a condenser, it is necessary to know the mass flow rate and molecular weight of the NCG, as well as the suction pressure, discharge pressure, gas suction temperature, mass flow rate of the water vapor, and steam pressure (Geothermal Institute 1996). Figure 8 shows the stage ejector flow diagram. To calculate the mass flow rate of the extraction gas and steam required for the SJE, the steps below should be followed:

1. Calculate the gas volume and mass flow rates of vapor water using *Dalton's laws of partial pressure* and the *ideal gas equations.* In the situation where water vapor saturates NCG, the gas volume flow rate ($\dot{V}$) is calculated thus:

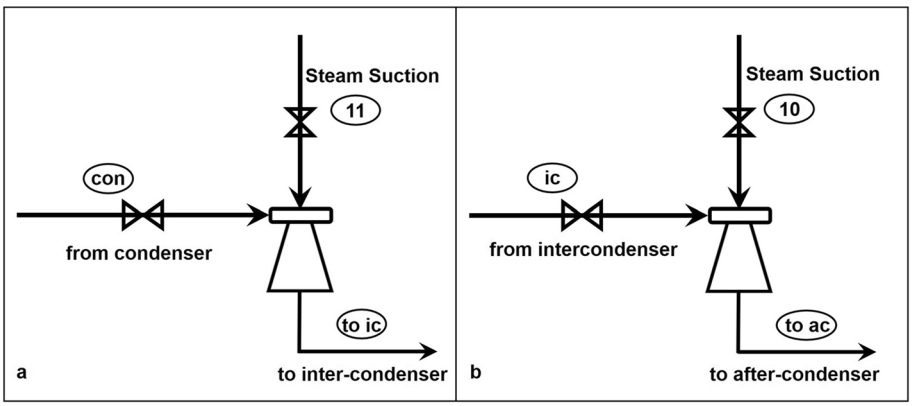

Fig. 8 Stage ejector flow diagram. The saturation pressure (P_t) of the hot gas and water vapor pressure (P_{wv}) in the system at a temperature of 25 ^{0}C is indicated by pressure at state 11 (P_{11}) as the first-stage ejector (**a**) and pressure at state 10 (P_{10}) as the second stage ejector (**b**)

$$\dot{V} = \frac{\left(\dot{m}\, RT\right)_{ncg}}{(P_t - P_{wv})}, \tag{15}$$

where P is pressure (N/m^2) and T is the temperature of the NCG (K).

The mass flow rate of the NCG to be discharged from the condenser is determined by the mass flow rate of the fluid entering the condenser. Each stage uses equal pressure ratios based on system suction and discharges a 90 % condenser pressure; 105 kPa, which is the permissible pressure drop, is 0.019 bar-a at the intercooler and aftercooler (Swandaru 2006).

2. Calculate the entrainment ratio using the equation generated from the entrainment ratio curve. Equation 16 can be used to compute the entrainment ratio of an NCG (E_{NCG}) :

$$E_{NCG} = \left[\left(5.73 \cdot 10^{-4} x 18.36\right) + \frac{(2.01 \cdot M_{NCG}^{0.86})}{(18.36. + M_{NCG}^{0.86})}\right]. \tag{16}$$

The water vapor entrainment ratio (E_{wv}) can be calculated using Eq. 17:

$$E_{wv} = \left[\left(5.73 \cdot 10^{-4} x 18.36\right) + \frac{(2.01 \cdot M_{wv}^{0.86})}{(18.36. + M_{wv}^{0.86})}\right]. \tag{17}$$

3. Calculate total air equivalent (TAE) using Eq. 18:

$$TAE = \frac{M_{NCG}}{E_{NCG}} + \frac{M_{wv}}{E_{wv}}. \tag{18}$$

4. Calculate compression ratio, which is defined as the ratio of discharge to suction, using Eq. 19:

$$\frac{P_{toic}}{P_{con}} = \frac{P_{toac}}{P_{ic}}, \tag{19}$$

where P_{con} is the pressure at the condenser, P_{toic} is the pressure before the inter-condenser, P_{ic} is the pressure at the inter-condenser, and P_{toac} is the pressure after the condenser.

5. Determine the expansion ratio (defined as the ratio of the motive steam pressure to the suction pressure) for the first (E_{r1}) and second (E_{r2}) stages using Eqs. 20 and 21:

$$E_{r1} = \frac{P_{11}}{P_{con}}, \tag{20}$$

$$E_{r2} = \frac{P_{ic}}{P_{toac}}. \tag{21}$$

6. Determine the air-to-steam ratio using the air-to-steam ratio curve.
To numerically approximate the air-to-steam ratio curve, digitized it for various compression ratio values and then logarithmically interpolate it to obtain a logarithmic equation for each compression ratio value in the air-to-steam ratio curve.

7. Determine motive steam mass flow rate at the first ($\dot{m}_{11}$) and second ($\dot{m}_{10}$) stages using Eqs. 22 and 23:

$$\dot{m}_{11} = \frac{TAE_1}{U_1}, \tag{22}$$

$$\dot{m}_{10} = \frac{TAE_2}{U_2}. \tag{23}$$

Assuming that the process is adiabatic (Q = 0) and the entire NCG (CO_2 in this case) is sucked in by the ejector, then the mass and energy balance of the ejector of stage 1 (h_{toic}) wIll be calculated using Eq. 24 and the mass and energy balance equations at stage 2 ejectors (h_{toac}) will be calculated using Eq. 25:

$$h_{toic} = \frac{\dot{m}_{con}h_{con} + \dot{m}_{11}h_{11}}{m_{toic}} = \frac{\dot{m}_{con}h_{con} + \dot{m}_{11}h_{11}}{\dot{m}_{con} + \dot{m}_{11}}, \tag{24}$$

$$h_{toac} = \frac{\dot{m}_{10}h_{10} + \dot{m}_{ic}h_{ic}}{m_{toac}} = \frac{\dot{m}_{10}h_{10} + \dot{m}_{ic}h_{ic}}{\dot{m}_{10} + \dot{m}_{ic}}. \tag{25}$$

The inter-condenser

The function of the inter-condenser is to condense the first-stage motive steam and remove part of the water vapor that initially saturated the NCG; it is shown in Fig. 9.

Assuming cold water absorbs all heat and there is no loss to the environment, the mass flow rate of the inter-condenser ($\dot{m}_{fromct}$) will be calculated using Eq. 26:

$$\dot{m}_{fromct} = \frac{\dot{m}_{toic}(h_{toic,vapor} - h_{tocon}) + \dot{m}_{toic,CO_2}(h_{toic} - h_{ic})_{CO_2} + \dot{m}_{ic,vapor}(h_{toic} - h_{ic})_{vapor}}{h_{tocon} - h_{fromct}}, \tag{26}$$

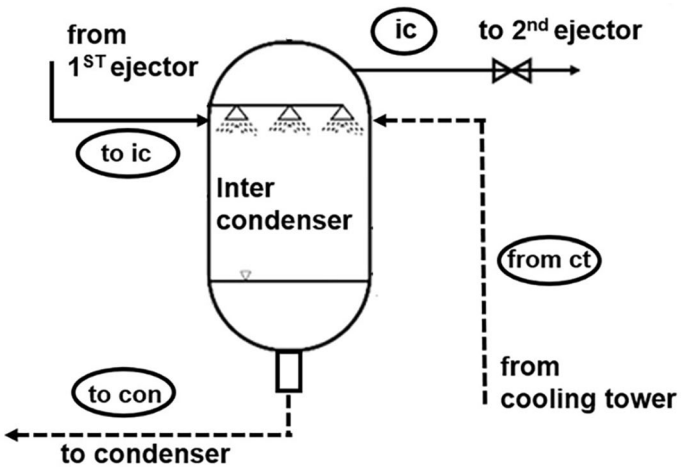

Fig. 9 The inter-condenser flow diagram

where $\dot{m}_{toic}$ is the mass flow rate before the inter-condenser, $\dot{m}_{toic,CO_2}$ is the mass flow rate of carbon dioxide before the inter-condenser, and $\dot{m}_{ic,vapor}$ is the mass flow rate of vapor at the inter-condenser.

Determining the mass balance equation in the inter-condenser is shown by Eq. 27:

$$\dot{m}_{tocon} = \dot{m}_{toic} + \dot{m}_{fromct} - \dot{m}_{ic}, \tag{27}$$

where $\dot{m}_{tocon}$ is the mass flow rate before the condenser and $\dot{m}_{ic}$ is the mass flow rate at the inter-condenser.

After-condenser

The after-condenser acts as the noise suppressor; the after-condenser process is shown in Fig. 10.

The formula for calculating the mass flow rate from the cooling tower at the second stage ($\dot{m}_{from\_ct2}$) is shown in Eq. 28:

$$\dot{m}_{from\_ct2} = \frac{\dot{m}_{toac}(h_{toac,v} - h_{tocon2}) + \dot{m}_{toac,CO_2}(h_{toac} - h_{aa})_{CO_2} + \dot{m}_{ic,v}(h_{ge} + h_{toac} - h_{ic})_v}{h_{tcon2} - h_{from\_ct2}} + E_{ge}, \tag{28}$$

where $\dot{m}_{toac}$ is the mass flow rate before the after-condenser and $\dot{m}_{toac,CO_2}$ is the mass flow rate of carbon dioxide before the after-condenser. The formula for calculating the energy at the gland ejector (E_{ge}) is shown in Eq. 29:

$$E_{ge} = \frac{\dot{m}_{ge,v}(h_{ge,uap} - h_{tocon2}) + \dot{m}_{ge,CO_2}(h_{ge} - h_{aa})_{CO_2}}{h_{tcon2} - h_{fromct2}}, \tag{29}$$

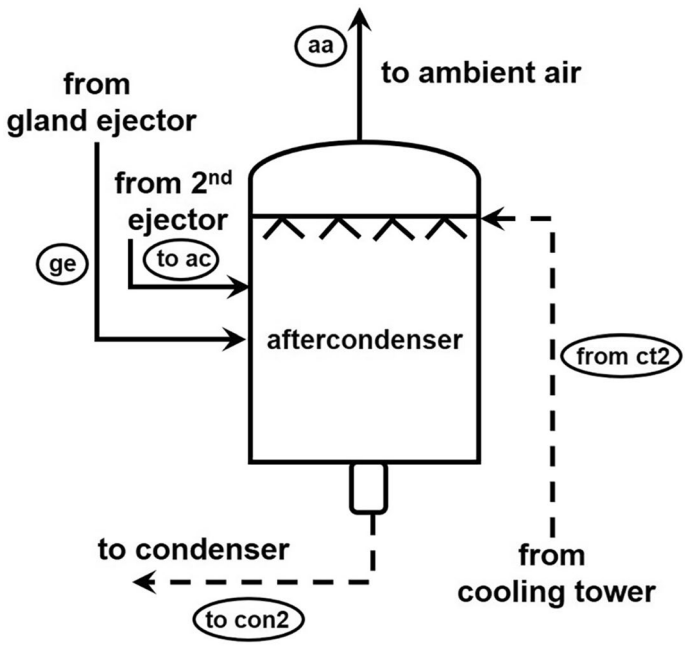

Fig. 10 The after-condenser flow diagram

where $\dot{m}_{ge,v}$ is the mass flow rate of vapor at the gland ejector, $\dot{m}_{ge,CO_2}$ is the mass flow rate of carbon dioxide at the gland ejector, $\dot{m}_{aa}$ is the mass flow rate of vapor at ambient air, h_{aa} is enthalpy at ambient air, h_{tocon2} is enthalpy before condenser, and $h_{fromct2}$ is enthalpy from the cooling tower. For determining the mass balance in the inter-condenser, Eq. 30 is used:

$$\dot{m}_{tocon2} = \dot{m}_{ge} + \dot{m}_{toac} + \dot{m}_{from\_ct2} - \dot{m}_{aa}. \tag{30}$$

The cooling tower

A wet cooling tower with a mechanical induction system will be used as the heat rejection system of the plant as shown in Fig. 11.

The energy balance equation for the cooling tower is shown below:

$$\dot{m}_a = \dot{m}_{a,ca1} = \dot{m}_{a,ca2} = \frac{\dot{m}_{toct}(h_{toct} - h_{topp})}{\left(h_{a,ca2} + \omega_{ca2}h_{v,ca2}\right) - \left(h_{a,ca1} + \omega_{ca1}h_{v,ca1}\right)}, \tag{31}$$

where $\dot{m}_a$ is the air mass at the cooling tower, $\dot{m}_{a,ca1}$ is the air mass from the cooling tower, $\dot{m}_{a,ca2}$ is the mass of exhaust air, $\dot{m}_{toct}$ is the mass flow rate from the HWP or condenser, h_{toct} is enthalpy from the condenser, h_{topp} is enthalpy to the condenser and primary pump, $h_{a,ca1}$ is cool air enthalpy, $h_{a,ca2}$ is the enthalpy of exhaust air, ω_{ca1} is specific humidity of cool air, and ω_{ca2} is the specific humidity of exhaust air. The value of specific relative humidity and air enthalpy is determined using the psychometric diagram.

The hot well pump (HWP)

The HWP is the main pump used to pump water from the condenser to the cooling tower for cooling. HWP power (W_{HWP}) can be calculated using Eq. 32:

$$W_{HWP} = \frac{g h_{headpump} m_{condensate}}{1000\eta_{pump}}, \tag{32}$$

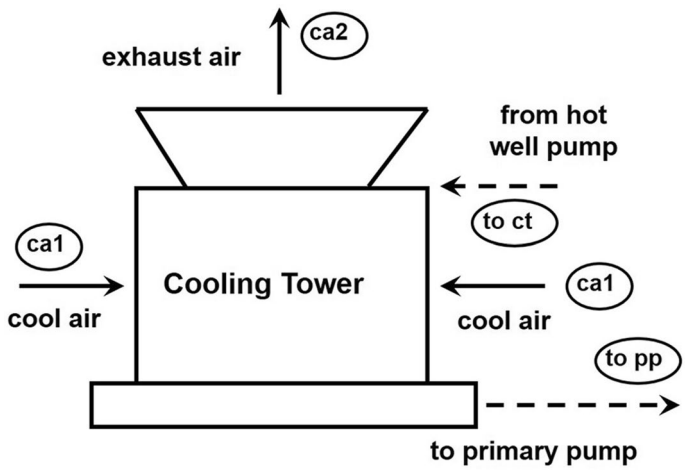

Fig. 11 The cooling tower flow diagram

where g is the gravitational constant, $h_{headpump}$ is a head pump, and η_{pump} is the pump efficiency.

The flow diagram for the mass and energy balance module is shown in Fig. 12. This figure shows the input and output parameters of each sub-module, and the sub-modules operate simultaneously, using the output parameters of each sub-module as input parameters for the others. The main power of the module are the net power, total auxiliary power of GPP, and SSC of the GPP. The module first identifies the optimum

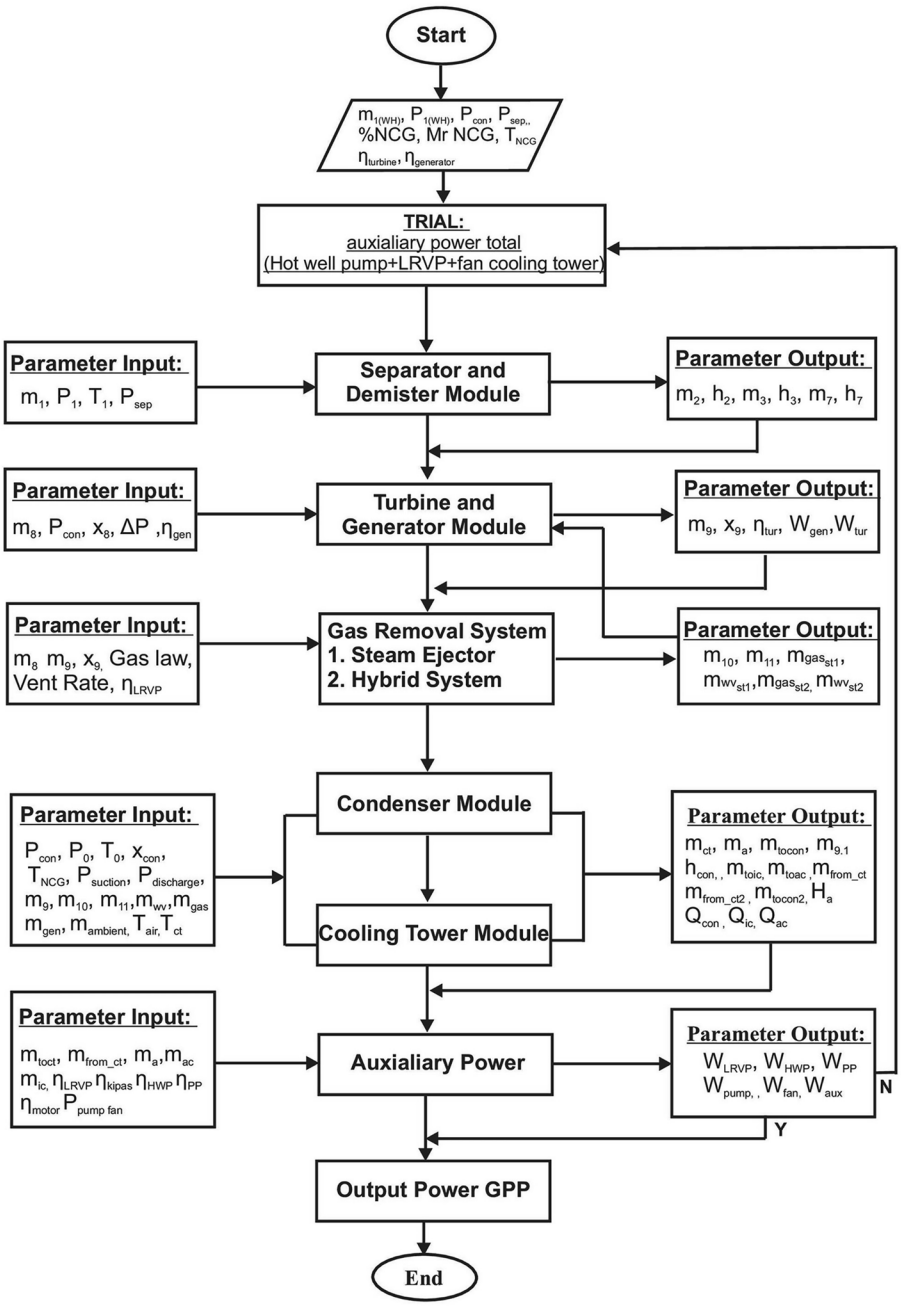

Fig. 12 Flowchart of the thermodynamical model of a single-flash GPP

separator and condenser pressures that give the maximum net power output and minimum total auxiliary power; it then calculates net power production and total auxiliary power for NCG removal systems using optimum separator and condenser pressures. This module also determines the mass flow rate, enthalpy, temperature, and pressure at each GPP state.

Results and discussion

The first step of modeling is analyzing the heat and mass balance of every vessel of GPP Units 2 and 3 (SJE) and Unit 4 (HS).

The ejector system

Our model was only validated with the annual average electricity production capacity (net power output) of Kamojang GPP Units 2 and 3, both of which use compressors as an NCG removal system. Data were used in calculating the output power of the second and third units of the Kamojang GPP, as shown in Table 1.

The GPP input interface of the mass and energy balance module is shown in Fig. 13.

In our model, when the Run Button was clicked, it displayed output specifications of each GPP module, such as turbine data, generator data, gas extractor data, condenser, inter-condenser, after-condenser, cooling tower, and pump in the list box and SI unit, shown in Fig. 14, the screen results for Kamojang Units 2 and 3-type ejector systems (Fig. 15), and the screen results for Kamojang Units 2 and 3-type HSs (Fig. 16). The results of the comparison and validation of our model's data with those of GPP Kamojang Units 2 and 3 using an ejector system are shown on Table 2.

The model was validated using the construction data of the mass and energy balance of Kamojang GPP's Units 2 and 3 (100% load). The model was then validated using both process flow diagram (PFD) and daily operational data. The minimum error expected in this calculation was 5%. The validation results showed that the

Table 1 Data and assumptions of Kamojang GPP Units 2 and 3

Parameter	Value	Unit
Wellhead pressure (P_1)	34	bar-a
Mass flow rate (m_1)	390060	kg/h
Separator outlet enthalpy (h_2)	2759.5	kJ/kg
Turbine inlet temperature (T_8)	161.9	°C
Turbine outlet pressure (P_9)	0.1	bar-a
Turbine outlet temperature, (T_9)	45.8	°C
Mass flow rate of vapor, (m_{vapor})	376580	kg/h
Mass flow rate of CO_2, (M_0 CO_2)	1883	kg/h
Molecular weight total	42.9	kg/kmol
Static pressure total	6.7	mmH_2O
Velocity pressure	4.7	mmH_2O
Cooling tower temperature	27	°C
Suction pressure	0.41	bar-a
1st ejector suction pressure	29	°C
2nd ejector suction pressure	40	°C
After-condenser outlet temperature	50	°C

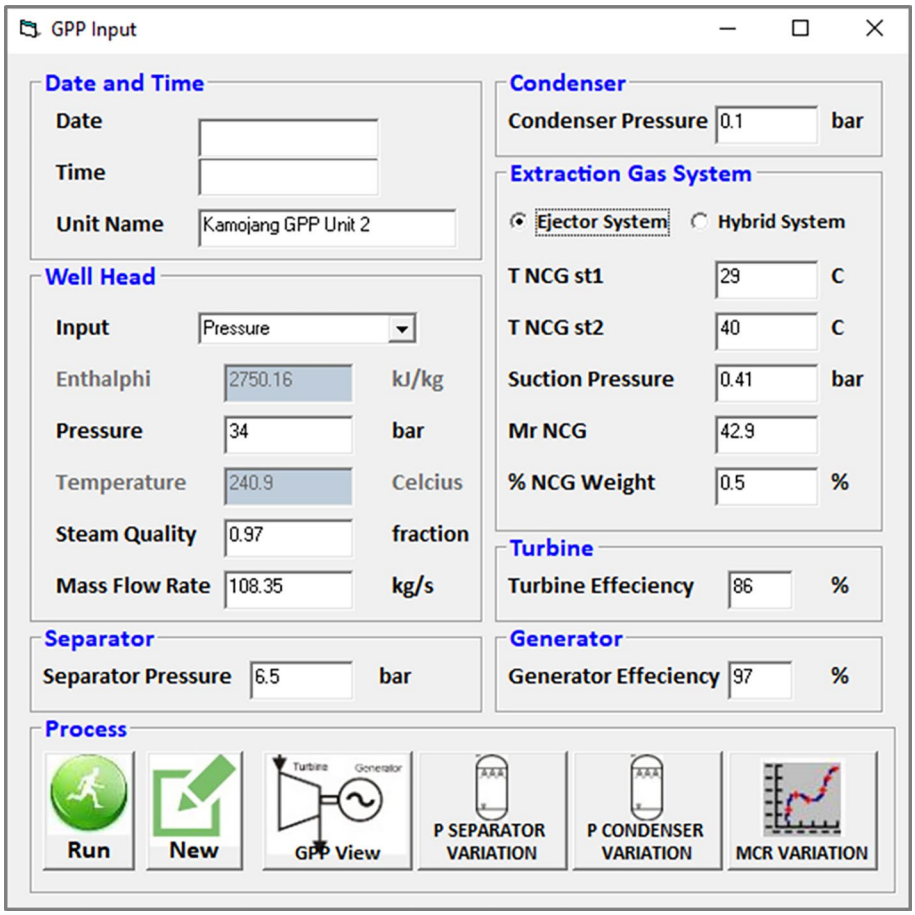

Fig. 13 An input interface of the single-flash Kamojang GPP

generator output of our model was 55.294 MW, a difference of approximately 0.53% (0.2 MW) compared to that of the design data used for the Kamojang GPP's Units 2 and 3, which generate 55 MW generator output. The specifications of other components also had an error of < 5%. Since the calculation error was < 5%, this model is considered valid for use in the simulation. Based on the results on Table 2, the total steam required to generate a net power output of 55 MW using the HS (384408 kg/h) is lower than that required to generate the same net power output using the ejector system (388944 kg/h). Therefore, the HS saves 4536 kg/h of steam, an equivalent of 693 kW of power, because the HS requires less motive steam to attract NCGs. Regarding auxiliary energy consumption, that of the HS was higher than that of the ejector system; for a net power output of 55 MW, auxiliary power consumption from the HS was 1313 kW while that for the ejector system was 1154 kW. The difference in auxiliary power consumption of 159 kW is equivalent to the amount of electric power installed by the LRVP when using an HS. When the amount of LRVP power (159 kW) that needs to be added to the HS is subtracted from the 693 kW of power it saves, the total amount of steam saved by the HS is 534 kW or 0.97% of the power output. Horas et al. (2017) also stated that based on the thermodynamic model in the Darajat GPP's Unit 3, the HS can save energy by 1.11% compared to SJE.

Geothermal Power Plant Spesification

No	Spesification	Unit	Type/Value	Type/Value
1	Turbine data		Ejector System	Hybrid System
	Rated Capacity	KW	57005	57128
	Steam Inlet Pressure	bar	6,49	6,49
	Steam Temperature	celcius	161,93	161,93
	Non Condesable Gas	% weight	0,5	0,5
	Steam Flow Rate	kg/s	105,13	105,35
	Turbine Effeciency	%	86	86
2	Generator Data			
	Rated Capacity	kW	55295	55414
	Generator Effeciency	%	97	97
3	Gas Extractor data			
	Type		Ejector System	Hybrid System
	First Stage		Steam Ejector	Steam Ejector
	Temperature First Stage	Celcius	25	25
	First stage motive steam flowrate	kg/s	1,65	1,43
	First stage gas mass flowrate	kg/s	0,53	0,53
	First stage gas volume flowrate	cub-m/s	5,14	5,15
	First stage water vapour mass flowrate	kg/s	0,15	0,15
	Second stage type		ejector system	hybrid system
	Second stage redundancy type		Steam Ejector	LRVP
	Temperature Second Stage	Celcius	40	--
	Second stage motive steam flowrate	kg/s	1,26	--
	Second stage gas mass flowrate	kg/s	0,65	--
	Second stage gas volume flowrate	cub-m/s	1,18	--
	Second stage water vapour mass flowrate	kg/s	0,06	--
4	Condenser Data			
	Type		Direct Contact	Direct Contact
	Pressure	bar-a	0,1	0,1
	Temperature	°C	45,81	45,81
	Enthalphi	KJ/kg	2337	2337
	Inlet Cooling Water Mass Flow	kg/s	3466	3493
	Outlet Cooling Water Mass Flow	kg/s	3658	3691
5	Intercondenser Data			
	Pressure	bar-a	0,41	0,41
	Inlet Cooling Water Mass Flow	kg/s	41,83	42,31
	Outlet Condenser Mass Flow	kg/s	43,57	43,85
6	Aftercondenser Data			
	Pressure	bar-a	0,95	0,95
	Inlet Cooling Water Mass Flow	kg/s	41,93	42,35
	Outlet Condenser Mass Flow	kg/s	43,52	44,15
7	Cooling Tower			
	Cooling Tower Type		Mechanical Draft	Mechanical Draft
	Inlet Cooling Water Mass Flow	kg/s	3639	3695
	Dry Air Mass Flow	kg/s	3492	3514
	Fan Power	kW/cell	115	168
8	Pump			
	Pump Type		MCWP	MCWP
	MCWP Power (V.dp)	kW	1118	1274
	MCWP Power (A.h)	kW	916	1044
	Pump Type		Primary Pump	Primary Pump
	Primary Pump Power (V.dp)	kW	36	39
	Primary Pump Power (A.h)	kW	32	35

Fig. 14 Output of specification Kamojang GPP Units 2 and 3

Figure 17 shows a graph of the effect that NCG in the range of 0 to 20% has on the turbine output. The figure indicates that net power output decreases with increasing NCG fraction. The SJE has a dramatic decrease in net power output by NCG fraction compared to the HS. A 1% increment in NCG fraction results in a decrease in net power output of 2.03% for the SJE and 1.6% for the HS. Therefore, the separation pressure is very important to maximize the net power output. This is consistent with the findings of a study by Ozcan and Gokcen (2013) which was based on thermodynamic calculations using the EES at GPP Kizildere-Turkey; they had concluded that for every 1% increase in NCG concentration in steam, there is a 2.2% decrease in NCG concentration in steam for the HS and a 2.7% decrease for the SJE. The use of steam for the SJE and HS is nearly identical at a pressure of 0.1 bar-a in a steam condition of 0.5 to 1.5% NCG fraction.

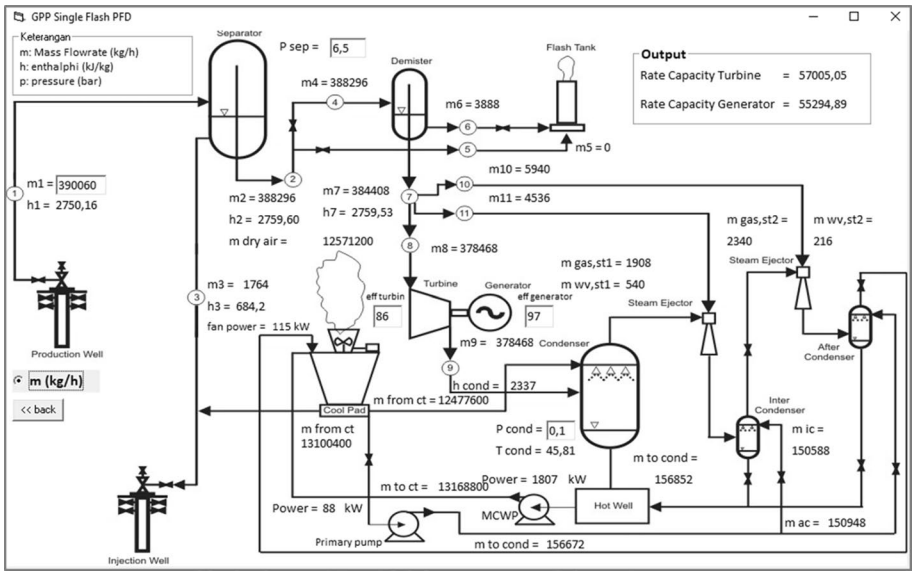

Fig. 15 Screen results of Kamojang Units 2 and 3 types of ejector systems

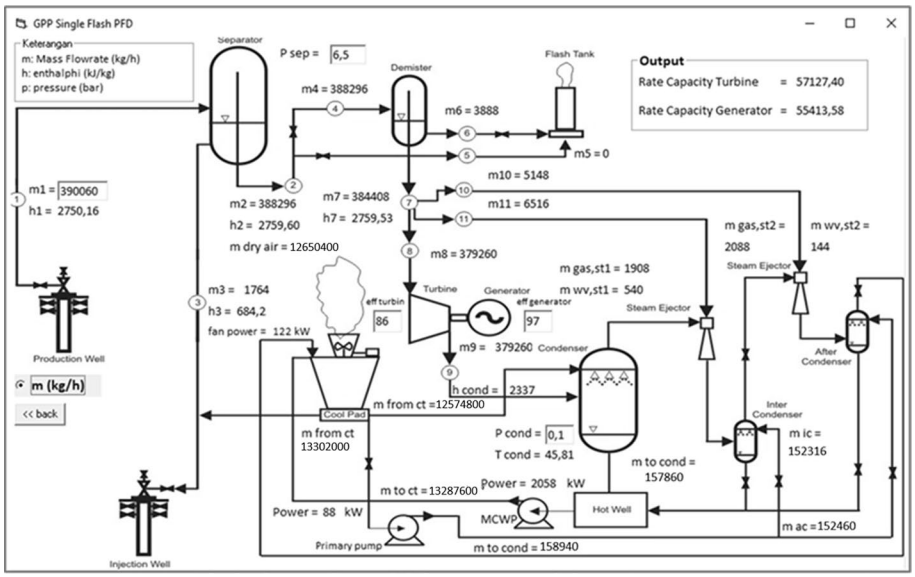

Fig. 16 Screen results Kamojang Units 2 and 3 types of HSs

Marza (2011) confirmed this finding in his research where he found that at a vapor condition of 0.08 bar-a at a high NCG fraction (NCG > 1.5%), the SJE required roughly three times as much motive steam as the HS.

The hybrid system

Data used in calculating the output power of the Kamojang GPP Unit 4 are shown in Table 3.

Table 4 also shows the results of the comparison and validation of our model data with the design data of Kamojang GPP's Unit 4 using an HS.

Table 2 Validation results of Kamojang GPP Units 2 and 3

Specification	Unit	Component	Design data	Ejector model	*Hybrid model*
Rated capacity	kW	Turbine	55000	55295	55413
Steam flowrate	kg/h		376580	378468	379260
Inlet cooling water mass flow rate	kg/h	Inter-condenser	150000	150588	152316
Outlet condensate mass flow rate	kg/h		156419	156852	157860
Inlet cooling water mass flow rate	kg/h	After-condenser	150000	150948	152460
Outlet condensate mass flow rate	kg/h		155542	156672	158940
Inlet cooling water mass flow rate	kg/h	Condenser	12488135	12477600	12574800
Outlet condensate mass flow rate	kg/h		1300000	13168800	13287600
Enthalpy	kJ/kg		2218.6	2218	2218
Inlet cooling water mass flow rate	kg/h	Cooling tower	13200000	13100400	13302000
Suction steam rate	kg/h	Ejector 1	5900	5940	5148
Suction steam rate	kg/h	Ejector 2	4560	4535	6516
MCWP power	kW	MCWP	860	916	1044

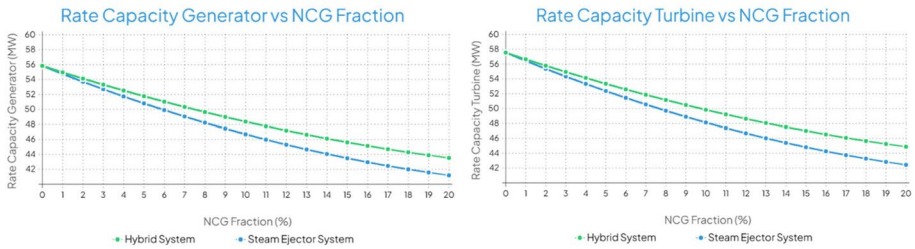

Fig. 17 Rate capacity generator and turbine vs NCG Fraction

Table 3 Data and assumptions of Kamojang GPP's Unit 4

Parameter	Value	Unit
Wellhead pressure (P_1)	34	bar-a
Mass flow rate (m_1)	417600	kg/h
Separator outlet enthalpy (h2)	2780.67	kJ/kg
Turbine inlet temperature (T8)	11	bar-a
Turbine outlet pressure (P9)	0.16	bar-a
Mass flow rate of vapor, (m_{vapor})	7120	kg/h
Molecular weight total	42.9	kg/kmol

The model was validated using the mass and energy balance design data of GPP Kamojang Unit 4 (100% load). The validation results showed that the generator output of our model was 60,218 MW, a difference of approximately 0.36% (0.2 MW) compared to the design data of the GPP Kamojang's Unit 4, which generates an output of 60 MW. The specifications of other components also had an error of < 5%. Sasradipoera (2000) reported that the wells in the Kamojang geothermal field show a 5% decrease in production per year. Given this decline in production from the wells in the Kamojang geothermal field, it can be said that the use of an HS will extend the life of the wells as this GRS saves more steam.

Table 4 Validation results for our model using data from Kamojang GPP's Unit 4

State	Unit	Component	Data design	Data model	*Error* (%)
Rated capacity	kW	Turbine	60000	60218	0.36
Steam flowrate	kg/h		411729	411228	− 0.12
Inlet cooling water mass flow rate	kg/h	Inter-condenser	565999	565236	− 0.13
Outlet condensate mass flow rate	kg/h		578483	575460	− 0.52
Inlet cooling water mass flow rate	kg/h	After-condenser	–	672120	–
Outlet condensate mass flow rate	kg/h		–	684360	–
Inlet cooling water mass flow rate	kg/h	Condenser	7,381,203	7387200	0.08
Outlet condensate mass flow rate	kg/h		8384034	8359200	− 0.30
Enthalpy	kJ/kg		-	2221	–
Inlet cooling water mass flow rate	kg/h	Cooling tower	8194420	8247600	0.65
Suction steam rate	kg/h	Ejector 1st	9531	9648	1.23
Suction steam rate	kg/h	Ejector 2nd	–	12240	–
MCWP power	kW	MCWP	60000	60218	0.36

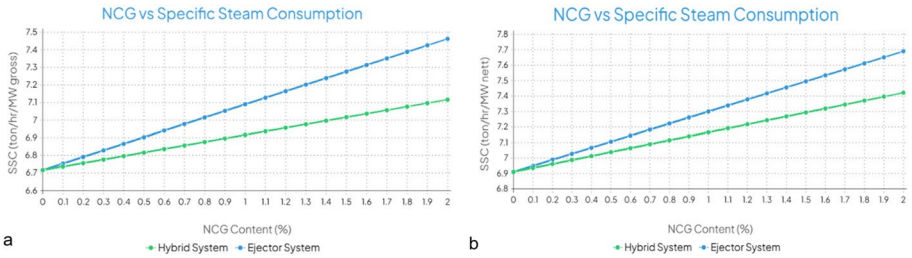

Fig. 18 Graphs of the effect of NCG content on SSC of each type of GRS **a** SSC_{gross} **b** SSC_{nett}

In this research, a sensitivity analysis of several factors influencing the selection of a GRS was performed. The factors analyzed were the amount of NCG content, turbine inlet pressure or steam drive pressure, and condensing pressure. One of the parameters commonly used to express the performance of a GPP is the amount of specific steam (SSC) consumed by the GPP. The SSC can be expressed as a ratio between the amount of steam available and the power generated. Figure 18(a) is a graph showing the relationship between NCG content and gross SSC for each type of GRS. Here, SSC_{gross} is the amount of specific steam consumed to produce gross turbine power from each GRS. The gross turbine power of the HS is greater than that of the ejector system because the HS requires more auxiliary power to drive the LRVP. Figure 18(b) shows the relationship between the NCG content and the SSC_{nett} of each type of GRS. SSC_{nett} is the net power produced by the generator after subtracting the auxiliary power. Based on Fig. 18a, b, it can be concluded that the total steam consumption for the generation of GPP is more efficient with the HS than with the ejector system, taking into account the auxiliary energy. The amount of LRVP power required by the HS to remove an amount of NCG remains less than the amount of power that can be generated by the motive steam, which the ejector requires to remove the same amount of NCG.

Figure 19a, b shows the relationship between the turbine inlet pressure of SSC_{gross} and that of SSC_{nett} for each GRS type. In GPPs, the properties of the motive steam (P, T) entering the ejector are usually the same as those of the steam entering the turbine.

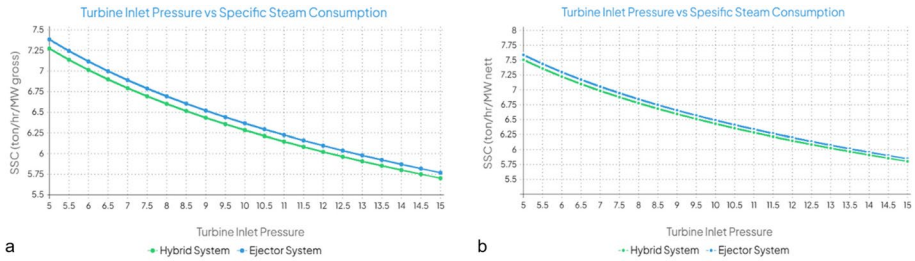

Fig. 19 Graphs of the effect of turbine inlet pressure on SSC of each type of GRS **a** SSC_{gross} **b** SSC_{nett}

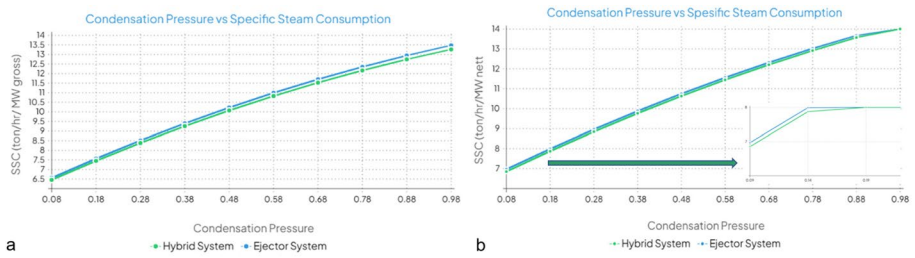

Fig. 20 Graphs showing the effect of condensation pressure on SSC for each type of GRS **a** SSC_{gross} **b** SSC_{nett}

The higher the motive steam pressure, the lower the motive steam flow rate required to remove the NCG, and also the greater the kinetic energy contained in the motive steam; thus, the motive steam requires a lower flow rate to remove NCGs. In addition, the decrease in enthalpy in the turbine becomes greater with a higher motive steam pressure; thus, the steam throughput required to generate electricity decreases for the same output. In Fig. 18a, b, it can be seen that the greater the turbine inlet pressure, the lesser the SSC required by each type of GRS; this reduces the required SSC. The HS has a lower SSC (both $SSC_{gross,}$ and SSC_{nett}) than the SJE.

Figure 20a, b are graphs illustrating the relationship between the condenser pressure of SSC_{gross} and that of SSC_{nett} for each type of GRS. From the figure, it can be seen that the greater the condenser pressure, the greater the SSC required by each type of GRS, and that the HS has a lower SSC than the ejector system, both $SSC_{gross,}$ and SSC_{nett}. From the results of the sensitivity analysis, it can be concluded that the SSC_{gross} required by the HS in each range of NCG content, turbine inlet pressure, and condenser pressure is still lower than that required by the ejector system. Therefore, it can be concluded that the power requirement for LRVP remains less than the power that can be generated by the motive steam, which the ejector system requires to remove the same amount of NCG; therefore, based on the thermodynamic approach, in general, an HS is more efficient than an SJE.

Conclusions

In this research, we developed a thermodynamic model of a single-flash GPP involving NCG fraction with a software-based interface using the Visual Basic programming language because of the dearth of design and simulation software of GPP integrating NCG removal systems. This modeling scheme will be useful for testing GPP performance and selecting GRS. Alternatives to the modeled NCG removal system are the SJE and HS. The

model was validated by comparing its thermodynamic parameter output with the PFD of Kamojang GPP's Units 2 and 3 (which uses an SJE) and Unit 4 (which uses an HS). The validation of our model showed that the generator output of our model was 55.295 MW, a difference of approximately 0.53% (0.2 MW) compared to the PDF of Kamojang GPP's Units 2 and 3, and 60.218 MW, a difference of approximately 0.36% (0.2 MW) compared to the PFD of Kamojang GPP's Unit 4. Other component specifications also showed an error of < 5%; therefore, this model is considered valid for use in simulations. The selection of a GRS is very important as it depends on the amount of net power being generated. NCG fraction is the main variable influencing GPP performance, and the SJE is strongly influenced by an increase in NCG fraction since the steam flow motive to the SJE is directly related to the NCG fraction. The HS responds late to changes in NCG fraction, and LRVP is more efficient as its performance is between those of the compressor and SJE. Based on thermodynamic simulations, a 1% increment in NCG fraction results in a decrease in net power output of 2.03% for the SJE and 1.6% for the HS. Therefore, the separation pressure is very important to maximize the net power output. At a pressure of 0.1 bar-a, a steam condition of 0.5%, and an NCG fraction of 1.5%, the steam consumed by SJE and HS is almost the same. The total amount of steam needed to generate net power output at Kamojang GPP Units 2 and 3 is 55 MW using the HS, which is less than that needed by the ejector system because the HS requires less motive steam to attract NCG. In addition, the HS can save 693 kW of steam, but its steam consumption is 159 kW higher than that of the ejector system; therefore, the total steam it saves is 534 kW. From the results of the sensitivity analysis, it can be concluded that the LRVP power requirement is still less than the power that can be generated by the motive steam which the ejector requires to dispose of the same amount of NCG; therefore, GPP Kamojang Units 2 and 3 will be more efficient when an HS is used.

In general, the usage of the built modeling software on the generated power systems complies with the mass and energy balance calculation principles. The results have been validated with the output of thermodynamic parameters in the Kamojang PFD data. These results can be used to test the performance of the generating system and to recommend the selection of a gas removal system (GRS) that is suitable for the condition of the steam-containing NCG at the Kamojang GPP. This application can also be used to monitor the performance of the generating system and can be applied to other GPPs.

Acknowledgements
The authors would like to thank Pertamina Geothermal Energy of Kamojang, Laboratory of Modeling and Inversion, Physics of Earth and Complex System, ITB and Laboratory of Geothermal, Faculty of Petroleum and Mining, ITB for the permission to use their facilities for this study.

Author contributions
WS supervised the research. CMS conducted a field survey and retrieved thermal data. CMS and FTA developed the thermal model and designed the geothermal power plant (GPP) process flow diagram. CMS developed a Graphical User Interface (GUI) and code based on the thermal model of GPP involving Non-Condensable Gas. CMS and WS wrote the final manuscript. All authors read and approved the final manuscript.

Funding
This research was partially funded by Domestic Postgraduate Education Scholarships (BPPDN) provided by the Ministry of Education and Culture of the Republic of Indonesia, awarded to the first author.

Availability of data and materials
The data used in this study are available from the corresponding author, WS, upon reasonable request.

Declarations

Competing interests
The authors declare that they have no competing interests.

Received: 19 August 2022 Accepted: 1 March 2023
Published online: 20 March 2023

References

Agani M, Rozaq K, and Bachrun ZI. Construction and operation of Kamojang Unit 4, the First Commercial Geothermal Power Plant Built, Owned and Operated by PT Pertamina Geothermal Energy. In: Proceedings World Geothermal Congress 2010, Bali, Indonesia 25–29 April 2010.
Alimuddin T, Machfud AH, Novianto A. Preliminary analysis of single-flash geothermal power plant by using exergy method: a case study from Ulubelu geothermal power plant in Indonesia. Int J Renew Energy Res. 2018;8(3):1685.
Ameri M, Shamshirgaran SR, Pour Yousefi M. The study of key thermodynamic parameters effect on the performance of a flash steam geothermal power plant. In: Proceedings of 2nd Joint International Conference SEE 2006, Bangkok; 2006.
Aqui A, Aragones JS, Amistoso AE. Optimization of Palinpinon-1 production field based on exergy analysis-the southern negros geothermal field, Philippines. In: CD Proceedings of World Geothermal Congress, Paper No 1312, Antalya, Turkey. 2005. p. 1–7.
ASPEN-HYSYS Home Page. http://www.aspentech.com/core/aspen-hysys.cfm. Accessed 08 Jan 2022.
Assad MEH, Aryanfar Y, Radman S, Yousef B, Pakatchian M. Energy and exergy analyses of single flash geothermal power plant at optimum separator temperature. Int J Low Carbon Technol. 2021;16(3):873–81.
Bidini G, Desideri U, Maria F. A single flash integrated gas turbine-geothermal power plant with non-condensable gas combustion. Geothermics. 1999;28(1):131–50.
Bloomster CH, et al. GEOCOST: A computer program for geothermal cost analysis. No. BNWL-1888. Battelle Pacific Northwest Labs Richland Wash USA. 1975.
Cadenas R. Residual steam to energy: a project for Los Azufres geothermal field, Mexico. Geothermics. 1999;28:395–423.
Cengel Y, Boles MA. Thermodynamics an engineering approach. 9th ed. New york: McGraw-Hill; 2018.
Cerci Y. Performance evaluation of a single-flash geothermal power plant in Denizli, Turkey. Energy. 2003;28:27–35.
Chen L, Wang Y, Xie M, Ye K, Mohtaram S. Energy and exergy analysis of two modified adiabatic compressed air energy storage (A-CAES) system for cogeneration of power and cooling on the base of volatile fluid. J Energy Storage. 2021;42:103009.
Chung J, et al. Pre-economic analysis of Seokmo Island power generation with geothermal electricity technology evaluation model (GETEM). J Korean Soc Miner Energ Resour Eng. 2010;267–76.
Coury G, Guillen HV, Cruz DH. Geothermal noncondensable gas removal from turbine inlet steam. In: Proceedings 31st Intersociety 3 Energy Conversion Engineering Conference; 1996.
Dagdas A, Ozturk R, Bekdemir S. Thermodynamic evaluation of Denizli Kizildere geothermal power plant and its performance improvement. Energy Convers Manag. 2005;46:245–56.
DiPippo R. Thermodynamic improvements on the direct-steam plant. Trans Geotherm Res Counc. 1992;16:547–52.
DiPippo R. Second law analysis of flash-binary and multilevel binary geothermal power plants. Trans Geotherm Res Counc. 1994;18:505–10.
DiPippo R. Second law assessment of binary plants generating power from low-temperature geothermal fluids. Geothermics. 2004;33:565–86.
DiPippo R. Geothermal Power Plants: Principles, Applications, Case Studies and Environmental Impact: Fourth Edition. Geotherm Power Plants Princ Appl Case Stud Environ Impact Fourth Ed. 2015. 1–762.
DiPippo R, Marcille DF. Exergy analysis of geothermal power plants. Trans Geotherm Res Counc. 1984;8:47–52.
Duthie RG, Nawaz M. Comparison of direct contact and kettle reboilers to reduce non-condensables in geothermal steam. Trans Geotherm Res Counc. 1989;13:575–80.
El Wakil: Power Plant Technology. McGraw Hill Book; 1985.
Geothermal Institute. Gas extraction system. Course notes of Geothermal Institute, Auckland University, Diploma course in energy technology (geothermal). 1996;75.
Gokcen G, Yildirim N. Effect of non-condensable gases on geothermal power plant performance. Case study: Kizildere geothermal power plant-Turkey. Int J Exergy. 2008;5(5–6):684–95.
Hall NR. Gas extraction system. In: Dunstall MG (ed.) Geothermal utilisation engineering lecture notes. Geothermal institute, The University of Auckland, New Zealand; 1996.
Harvey W, Wallace K. Flash steam geothermal energy conversion systems: Single-, double-, and triple-flash and combined-cycle plants. Geotherm Power Gener Dev Innov. 2016. https://doi.org/10.1016/B978-0-08-100337-4.00010-3.
Horas R, Darmanto PS, Trirakhmadi A. Energy optimization and gas removal selection of geothermal power plant. In: 2017 International Conference on Sustainable Energy Engineering and Application (ICSEEA), Jakarta, Indonesia. 2017;25–33.
Jalilinasrabady S, Itoi R, Gotoh H, Kamenosono H. Energy and exergy analysis of Takigami geothermal power plant, Oita. Japan Trans Geotherm Resour Counc. 2010;34(2):966–71.
Jalilinasrabady S, Itoi R, Valdimarsson P, Saevarsdottir G, Fujii H. Flash cycle optimization of Sabalan geothermal power plant employing exergy concept. Geothermics. 2012;43:75–82.
Kanoglu M, Dincer I, Rosen MA. Understanding energy and exergy efficiencies for improved energy management in power plants. Energy Policy. 2007;35:3967–78.

Khalifa HE, Michaelides EE. The effect of noncondensable gases on the performance of geothermal steam power systems, Report of Brown University, Contract No EY-76-S-02–4051.1978.
Kwambai CB. Exergy analysis of Olkaria I Power Plant, Kenya, Reports of the United Nations University Geothermal Training Programme. Georgsson LS (ed.), ISBN 9979-68-183-7, Report No. 5, Reykjavik, Iceland. 2005.
Michaelides EE. Separation of noncondensables in geothermal installations by means of primary flashing. Trans Geotherm Res Counc. 1980;4:515–8.
Michaelides EE. The influence of non-condensable gases on the net work produced by the geothermal steam power plants. Geothermics. 1982;11(3):163–74.
Millachine T, Andrés M. Guidelines for optimum gas extraction system selection. Master thesis, Reykjavík, Iceland, University of Iceland. 2011.
Mohtaram S, Sun Y, Omidi M, Lin J. Energy-exergy efficiencies analyses of a waste-to-power generation system combined with an ammonia-water dilution Rankine cycle. Case Stud Thermal Eng. 2021;25:100909.
Montero G. Evaluation of the network of a turbine operated by a mixture of steam and non-condensable gases, Proc. 12th New Zealand Geothermal Workshop 1990. 1990;11:163–174.
Moran M, Saphiro M, Boettner D, Bailey M. Fundamental of engineering thermodynamics. 7th ed. Hoboken: John Wiley & Sons; 2011.
Moya D, Aldás C, Kaparaju P. Geothermal energy: power plant technology and direct heat applications. Renew Sustain Energy Rev. 2018;94:889–901.
Nasruddin, Idrus AM, Daud Y, Surachman A, Sugiyono A, Aditya HB, et al. Potential of geothermal energy for electricity generation in Indonesia: a review. Renew Sustain Energy Rev. 2016;53:733–40.
Omidi M, Liu S-J, Mohtaram S, Lu H-T, Zhang H-C. Improving centrifugal compressor performance by optimizing the design of impellers using genetic algorithm and computational fluid dynamics methods. Sustainability. 2019;11:5409.
Ozcan NY, Gokcen G. Performance analysis of single-flash geothermal power plants: gas removal systems point of view. In: Proceedings World Geothermal Congress 2010, Bali, Indonesia 25-29 April 2010.
Ozcan NY, Gokcen G. Performance analysis of single-flash geothermal power plants: Gas removal systems point of view. Geotherm Energy, Technol Geol. 2013;227–60.
Ozturk HK, Atalay O, Yilanci A, Hepbasli A. Energy and exergy analysis of kizildere geothermal power plant, Turkey. Energy Sources. 2006;23:1415–24.
Pambudi NA, Itoi R, Jalilinasrabady S, Jaelani K. Exergy analysis and optimization of Dieng single-flash geothermal power plant. Energy Convers Manage. 2014;78:405–11.
Pambudi NA, Itoi R, Jalilinasrabady S, Jaelani. Performance improvement of single-flash geothermal power plant applying three cases development scenarios using thermodynamic methods. In:Proceedings World Geothermal Congress, Bali, Indonesia 2015. 2015.
Rudiyanto B, Bahthiyar MA, Pambudi NA, Widjonarko HM. An update of second law analysis and optimization of a single-flash geothermal power plant in Dieng. Indonesia Geotherm. 2021;96:102212.
Sasradipoera DS, Sujata IK, Komaruddin U. Evaluation of steam production decline in the Kamojang geothermal field. In: Proceeding World Geothermal Congress, Japan. 2000.
Siregar, PHH. Optimization of Electrical Power Production Process for the Sibayak Geothermal Field, Indonesia, Report of the United Nations University Geothermal Training Programme Report No 16, Reykjavik, Iceland. 2004; 349–76.
Sulistyardi HB. Basic design of Lumut Balai 2x55 MW geothermal power plant The United Nations University. Indonesia: Geothermal Training Program; 2010. p. 615–24.
Swandaru RB. Thermodynamic Analysis of Preliminary Design of Power Plant Unit I Patuha, West Java, Indonesia, Report of the United Nations University Geothermal Training Programme Report No 7, Reykjavik, Iceland. 2006; 83–119.
Tajima S, Nomura M. Optimization of non-condensable gas removal system in geothermal power plant. Geotherm Res Council Trans. 1982;6:397–400.
Tomarov GV, Shipkov AA. Modern geothermal power: GeoPP with geothermal steam turbines. Therm Eng. 2017;64(3):190–200.
Triyono S. Thermodynamic and economic assessment of power plant expansion from 140 to 200 mw in Kamojang—Indonesia, report of geothermal training programme, Report No: 14. Reykjavik: The United Nations University; 2001.
Vorum M, Fitzler E. Comparative analysis of alternative means for removing noncondensable gases from flashed-steam geothermal power plants. United States. 2000.
Wahyuningsih R. Potensi Dan Wilayah Kerja Pertambangan Panas Bumi Di Indonesia, F. Results Colloq. - Cent. Coal Geothermal. Miner Resour. 2005;1–9.
Wang H, Yan G, Tag-Eldin E, Chaturvedi R, Aryanfar Y, Luis García Alcaraz J, et al. Thermodynamic investigation of a single flash geothermal power plant powered by carbon dioxide transcritical recovery cycle. Alexandria Eng J. 2022;64:441.
Yildirim ED, Gokcen G. Exergy analysis and performance evaluation of kizildere geothermal power plant, Turkey. Int J Energy. 2004;1:316–33.
Zarrouk SJ, Moon H. Efficiency of geothermal power plants: a worldwide review. Geothermics. 2014;51:142–53.

Publisher's Note